JOURNAL OF SPACECRAFT AND ROCKETS
Vol. 47, No. 6, November–December 2010

Hot-Gas Side Jet in a Supersonic Freestream

Bernhard Stahl,* Frank Siebe,† and Ali Gülhan‡
DLR, German Aerospace Center, 51147 Cologne, Germany

DOI: 10.2514/1.43670

The present paper reports on the interaction of a hot side jet in a supersonic freestream and compares the effects with results from cold-gas jet investigations. With high-speed schlieren videos, a significant enlargement of the separation area has been ascertained upstream from the hot-gas jet and quantitatively confirmed with wall pressure measurements. The schlieren videos also show a strong oscillation of the separation and bow shock. By using an algorithm that analyzes the similarity of neighboring images, the oscillation frequency of the separation and bow shock has been measured to be 11.3 kHz. As a consequence of the dominant shocks in the area in front of the jet, the hot jet plume is screened off strongly from the freestream, thus resulting in an upstream inclination. Finally, high-speed videos have revealed large-scale structures in the hot-gas jet and their convection velocities have been analyzed. According to the shocks, the large-scale structures oscillate at 11.3 kHz. Jet oscillation is thus excited by the interaction of the hot-gas jet with the freestream and not by resonances from the combustion chamber.

Nomenclature

A_J	=	jet exit area, m^2
$C_{p\text{dif}}$	=	differential pressure coefficient, measured with and without jet flow
D	=	diameter of the cylindrical part of model, mm
d_J	=	diameter of jet nozzle, mm
d_W	=	diameter of wind-tunnel nozzle, mm
F	=	jet exit thrust, N
I	=	jet exit momentum flux, N
M_J	=	Mach number of the side jet
M_∞	=	Mach number of the freestream
n	=	number of frames
p	=	local pressure, bar
p_t	=	total pressure of the freestream, bar
p_{tC}	=	total pressure of cold-gas jet in the chamber, bar
p_{tH}	=	total pressure of hot-gas jet in the combustion chamber, bar
p_∞	=	static pressure of the freestream, bar
Re_D	=	Reynolds number based on the model diameter D
T_{JC}	=	temperature of cold jet, K
T_{JH}	=	temperature of hot jet, K
T_{tC}	=	total temperature of the freestream and cold jet flow, K
T_∞	=	static temperature of the freestream, K
U_c	=	convection velocity of jet flow, $m \cdot s^{-1}$
U_J	=	velocity of jet flow, $m \cdot s^{-1}$
U_∞	=	velocity of freestream, $m \cdot s^{-1}$
x	=	distance downstream from the model tip, mm
z	=	direction of jet flow, mm
α	=	angle of attack, deg
Δt	=	time between frames, μs
λ	=	angle of separation shock, deg
φ	=	circumferential angle, deg
Φ	=	convection angle, deg
κ	=	isentropic exponent
ρ	=	density, $kg \cdot m^{-3}$

Subscripts

J	=	jet exit condition
JC	=	cold jet
JH	=	hot jet
t	=	static condition
∞	=	freestream

Received 6 February 2009; revision received 23 September 2009; accepted for publication 28 September 2009.

*Research Scientist, Wind Tunnel Department, Institute of Aerodynamic and Flow Technology; bernhard.stahl@dlr.de.

†Research Scientist, Wind Tunnel Department, Institute of Aerodynamic and Flow Technology; frank.siebe@dlr.de.

‡Head of Department, Research Scientist, Wind Tunnel Department, Institute of Aerodynamic and Flow Technology; ali.guelhan@dlr.de. Member AIAA.

I. Introduction

THE controlled lateral injection of the side jet, particularly at low dynamic pressure (i.e., at high altitudes or during the launch phase), is a very effective means of control for missiles. Furthermore, this tool is ideal for missiles of high agility and maneuverability. By comparison, control systems with aileron and rudder work only at very high velocities and high densities.

The expansion of a jet injected at high pressure into the supersonic freestream generates an exceptionally complex flowfield that is difficult to predict and strongly dependent on such parameters as jet pressure ratio and stagnation pressure. Of prime importance here is the extent to which the forces induced by the side-jet exercise an influence on thrust. If, considered integrally, the overpressure area upstream from the jet exceeds the low-pressure area in the wake, the side-jet thrust is reinforced and we can speak of an amplification factor $K_F > 1$ [1–3].

The interaction area of cold side jets is characterized essentially by a separated area in front of the jet, by a bow shock generated immediately in front of the jet, and by counter-rotating vortex pairs in the wake. The jet plume itself is limited by a barrel shock and the Mach disk. Its inclination depends on the freestream velocity, on penetration depth in relation to the jet pressure ratio, and on altitude. The topology of the flowfield of cold side jets is depicted in [4–8].

Since the interaction area of cold side jets has been comprehensively investigated experimentally and numerically in several studies, this paper focuses in the following on the effects of hot side jets. Hot side jets are mostly generated with solid propellants or impulse cartridges and more rarely with gas generators or liquid-fuel engines. Impulse cartridges can only be ignited once and therefore have to be available in a large number to correct the trajectory of the rotating missile. Liquid-fuel engines are technically more complex, but have the advantage of repeated ignition with dosed side-jet blasts to achieve the required trajectory adjustment. On the Terminal High-Altitude Area Defense (THAAD) defense missile, for instance, electronically controlled valves are used for controlling propellant supply and hence burn time and thrust power [9]. Depending on the missile's angle of attack, reattachment may take place in the wake of

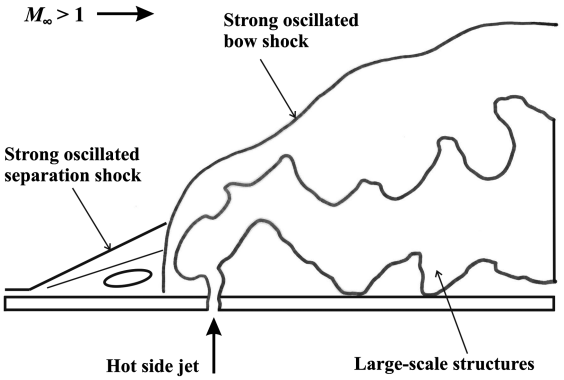

Fig. 1 Schematic view of lateral hot jet injection into a supersonic flowfield.

the hot-gas jet, and a fuselage material is thus required that withstands the thermal load. Esch [10] generated a hot-gas jet with a hydrazine engine and measured the resultant induced forces with a duct balance. For high supersonic Mach numbers and positive angles of attack, the quantitative force amplification factors show values of $K_F > 1$ and are higher than the factors obtained for cold-gas jets. Havermann et al. [3] numerically calculated the induced normal forces and amplification factors from wall pressure distributions in the interaction region of a hot side jet. The force amplification factors here show a considerable dependence on the angle of attack of the wind-tunnel model.

With measurements of wall pressure distributions on cold and hot side jets, the effects in the interaction area were published in [7]. The topology of the hot side jet represented schematically in Fig. 1 is derived from these analyses. By contrast with cold-gas jets, particularly noticeable is an enlargement of the area in front of the jet with considerably oscillation of the separation and bow shock. Because the jet is screened off from the freestream by the shocks, the jet plume of the hot jet inclines upstream. Moreover, with the aid of high-speed videos, large-scale structures were identified in a hot-gas jet and their convection velocities were determined. Naumann et al. [11] visualized the large-scale structures of a hot side jet with a laser light sheet. To illuminate the jet, titanium dioxide TiO_2 was used as seeding. As the results show, especially strong mixing phenomena on the windward side of the jet were detected. Mahmud and Bowersox [12] investigated the effect of a helium side jet with a low blowing ratio on the enlargement of the separated boundary layer in front of the jet. Helium was used to simulate higher temperatures because helium at ambient temperatures has nearly the same jet exit velocity and simulates air at approximately 2000 K [5]. As the results in [12–14] show, the separation distance in front of a helium jet increases much less than in the case of the high-temperature jet presented in this paper.

Until now, many experimental and numeric investigations with hot-gas jets have been primarily devoted to the interference of hot jets with the freestream in terms of an increase in side-jet thrust. Detailed studies into the topology of the hot-gas jet have been rarer. To fill this gap, the present paper reports particularly on the structure and development of hot-gas jets and compares this with the results from work on cold-gas jets.

II. Experimental Facility and Instrumentation

The experiments were carried out in the supersonic wind tunnel (VMK) in Cologne. The VMK wind tunnel is an intermittent blowdown tunnel for supersonic flows with a vertical open freejet test section and axially symmetrical fixed nozzles. The maximum blowdown duration is 60 s. The Mach number in the supersonic operation mode ranges from 1.57 to 3.2. The maximum total pressure is 35 bar and the overall temperature ranges from ambient temperature to 740 K. The Reynolds number based on a 1 m length ranges from $Re = 37 \times 10^6$ to 286×10^6.

Figure 2 shows a schematic view of the model setup. The model can be traversed in the x and y directions and in the range of the angle

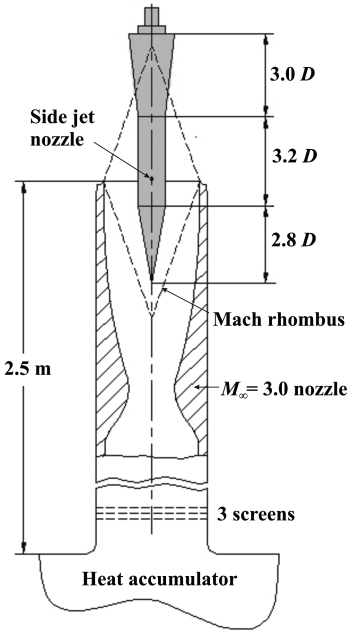

Fig. 2 Schematic view of model setup in the vertical freejet test section (VMK).

of attack of $-15° \leq \alpha \leq 15°$. The vertical position of the model was aligned according to the rhombuses of supersonic freestream.

A. Generic Missile Model

For the investigation of cold- and hot-gas jets, a generic wind-tunnel model was employed, which consists of the classical components of the cone, cylindrical fuselage, and flare (Fig. 3). For operation with hot gas, the wall thickness of the model was dimensioned for the expected combustion chamber temperature of 2300 K and the maximum combustion chamber pressure of 150 bar. Employed were solid propellants serving as the front combustor with a diameter of 72 mm and a length of 150 mm. The double-based propellants consisted of nitrocellulose and nitroglycerine and were ignited by a propellant ignition device. The burn time can be varied by using propellants of different lengths. After ignition, the hot gas

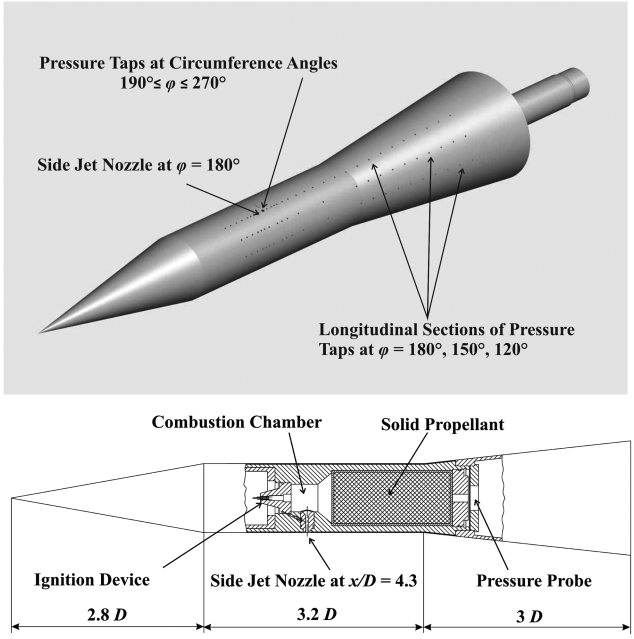

Fig. 3 Cone-cylinder-flare model with side-jet nozzle for cold- or hot-gas jet.

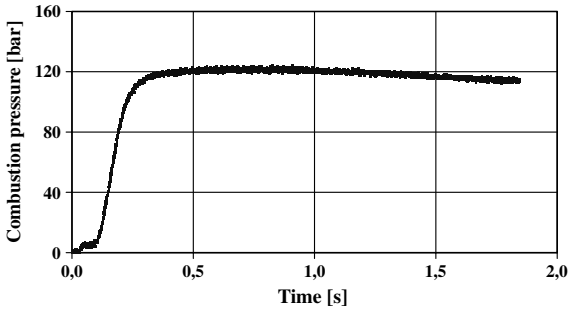

Fig. 4 Pressure into combustion chamber during propellant burning.

flows out of the combustion chamber into the molybdenum nozzle and generates the hot-gas jet. During propellant burn, the pressure was measured in the combustion chamber. For isotropic relaxation from 100 to 1 bar, the hot-gas jet is composed of 37.6% CO, (mass ratio %), 1.7% H_2, 1.1% Pb, 10.3%, H_2O, 34.9% CO_2, 13.9% N_2, and 0.3% Cu. For this gas composite, the isentropic exponent is $\kappa_H = 1.235$ and the gas constant is $R_H = 319\ \mathrm{J/kg \cdot K}$. For this it was assumed that the propellant gas is chemically inert. On this assumption, the gas constant is also constant over the entire condition range.

The diameter of the cylindrical fuselage component is $D = 90$ mm and its length $3.2D$; the model cone has a length of $2.8D$, and the flare has $3D$. The cylindrical jet nozzle is positioned at $\varphi = 180°$ and $4.3D$ downstream from the tip of the cone. At the exit of the nozzle, the Mach number of the cold- and hot-gas jets is $M_J = 1.0$. The exit temperature is $T_{\mathrm{JC}} = 244$ K for the cold jet and $T_{\mathrm{JH}} = 2058$ K for the hot jet. The pressure at the combustion chamber is $p_{\mathrm{tH}} = 120$ bar, due to the diameter of the nozzle $d_J = 4.6$ mm. Figure 4 shows the pressure distribution during the propellant burning. The measurements were carried out under the test conditions given in Table 1.

B. Pressure Measurements

To measure the pressure distribution on the model surface, the model has 93 static pressure taps with a diameter of 0.5 mm; 83 pressure taps are positioned in three longitudinal sections at the circumferential angles of $\varphi = 180$, 150, and 120°, and 10 taps are positioned at $x/D = 4.3$ in the angle range of $190° \le \varphi \le 270°$. For measurement of the wall pressure distributions, the pressure taps were connected to PSI modules (PSI 8400 System from Esterline). The static accuracy of the PSI modules is ±0.1% of the full-scale deflection. Measurement error due to Mach number deviations and changes in the freestream angle are generally greater in supersonic wind tunnels. In the VMK, local pressure deviations as a consequence of ΔM_∞ of $\Delta C_p = \pm 0.004$ and due to $\Delta\alpha$ deviations of $\Delta C_p = \pm 0.003$ can occur. The jet pressure ratios p_{tH}/p_∞ and p_{tC}/p_∞ can be generated by varying the static pressure p_∞ of the freestream.

Table 1 Test parameters

Parameter	Value
M_∞	3.0
M_J	1.0
d_W, mm	312
d_J, mm	4.6
T_{JC}, K	244
T_{tC}, K	293
T_∞, K	105
T_{JH}, K	2058
p_t, bar	20
p_∞, bar	0.545
p_{tH}, bar	120
p_{tH}/p_∞	220
$\rho_J \cdot U_J^2 \cdot A_J$, N	134

C. Flow Visualization

To video the gas jets, a high-speed camera was employed. The Photron Fastcam Ultima APX-RS camera can take 3 kfps with a resolution of 1024×1024 pixels. At reduced resolution, up to 250 kfps are possible. The camera operates with a 10-bit monochromatic C-MOS sensor.

For flow visualization in the VMK, a schlieren system in a standard Z arrangement was used. The light source consists of an arc lamp. Two $f = 3$-m-diam concave mirrors are employed to collimate the light through the test section and then refocus it into a knife edge. The test object is imaged with a lens onto a camera.

III. Experimental Results

A. Boundary Conditions of Side-Jet Measurements

The boundary conditions given in the literature on side-jet investigations are either the jet pressure ratio p_{tH}/p_∞, the momentum flux at jet exit $I = (\rho_{\mathrm{JH}} \cdot U_{\mathrm{JH}}^2) \cdot A_J = (\rho_{\mathrm{JC}} \cdot U_{\mathrm{JC}}^2) \cdot A_J$, the jet-to-freestream momentum flux ratio $(\kappa \cdot p \cdot M)_J/(\kappa \cdot p \cdot M)_\infty$, or the thrust $F = (\rho_{\mathrm{JH}} \cdot U_{\mathrm{JH}}^2 + p_{\mathrm{JH}} - p_\infty) \cdot A_J = (\rho_{\mathrm{JC}} \cdot U_{\mathrm{JC}}^2 + p_{\mathrm{JC}} - p_\infty) \cdot A_J$. For cold jets, the results are for the most part compared at the same jet pressure ratio and jet-to-freestream momentum flux ratio. Hot-gas jets at very high temperatures show a considerably higher exit velocity with lower densities. In that case, it is advisable to refer to the same momentum flux or thrust as the boundary condition. Table 2 compares the pressures at jet exit and of the model chamber for the momentum flux, the jet pressure ratio and the thrust of the cold- and hot-gas configurations. It can be seen that the biggest difference in chamber pressures is given with the same momentum flux. In this case, the hot-gas jet shows a factor 2.9 higher exit velocity and a factor 8.2 lower density. For the results presented in this report, the momentum flux at jet exit is defined as the boundary condition, as the calculation does not include any parameters of the freestream.

B. High-Speed Schlieren Measurements

To analyze the shocks of side jets without the freestream, high-speed schlieren videos were recorded. The camera settings for videos of the cold- and hot-gas jets were same: frame rate 3 kfps, resolution 1024×1024 pixels, and shutter exposure of 50 μs. Figure 5 compares the schlieren images measured at the same momentum flux of $(\rho_{\mathrm{JH}} \cdot U_{\mathrm{JH}}^2) \cdot A_J = (\rho_{\mathrm{JC}} \cdot U_{\mathrm{JC}}^2) \cdot A_J$. Independently of κ and the exit pressure ratios in the range of $15 \le p_{\mathrm{tC}}/p_\infty \le 17,000$, the distance from the Mach disk to the nozzle orifice according to [15] is

$$z_M/d_J = 0.67(p_{\mathrm{tC}}/p_\infty)^{1/2} \tag{1}$$

The calculated distance here is $z_M/d_J = 7.02$ and concurs well with the experimental result of $z_M/d_J = 6.91$ for the cold-gas jet. For the hot-gas jet, the lateral extension of $z_M/d_J = 6.85$ is slightly smaller, while the diameter of the Mach disk is approximately 15% larger. Only at the edge of the Mach disk is the barrel shock weakly visible. As a result of the considerable expansion of the hot-gas jet, there is a significant enlargement of the shear layer, causing the barrel shock in the schlieren image to be masked. The measured temperature difference between the hot-gas jet and its ambient surroundings is 1760 K [16].

Table 2 Boundary conditions of side-jet measurements

	$I = 134$ N ($M_J = 1.0$)	$p_{\mathrm{tH,tC}}/p_\infty = 220$ ($M_\infty = 3.0$, $M_J = 1.0$)	$F = 247$ N ($M_\infty = 3.0$, $M_J = 1.0$)
		Jet exit pressure	
p_{JH}, bar	66.9	66.9	66.9
p_{JC}, bar	59.0	63.4	65.6
		Chamber pressure	
p_{tH}, bar	120	120	120
p_{tC}, bar	112	120	124

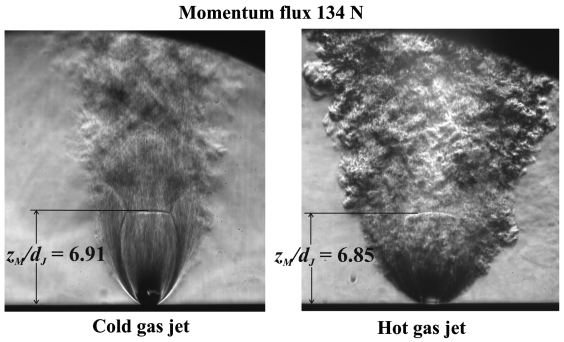

Fig. 5 Schlieren illustration of the expansion of cold- and hot-gas jets at $I = 134$ N and $d_J = 4.6$ mm.

To also investigate the local density changes in the cold-gas jet, measurements were carried out with the background-oriented schlieren (BOS) method. The advantage of BOS over conventional schlieren imaging is that density gradients in a flowfield can be determined with a simple experimental setup [17–20]. The physical effect exploited involves the deflection of light by density gradients orthogonal to the direction of light dispersion. For the application of BOS, a speckle pattern located in the background of the supersonic flow is recorded with a high-speed camera (in this case, with 3 kfps of 1024×1024 pixels). As a result of the density gradients of the flow, the speckle pattern is deflected and is proportional to the geometric sum of the density gradients $\mathrm{d}\rho/\mathrm{d}x$ and $\mathrm{d}\rho/\mathrm{d}z$. The cross-correlation of the speckle pattern (reference image without flow) with the image from the measurement then yields a two-dimensional density gradient field of the side jet.

Figure 6 shows the density gradients in the cold underexpanded side jet. The arrows indicate the intensity and direction of the density changes. Immediately after jet exit, significant density changes take place as a result of expansion. In the jet core, the density changes are considerably smaller and increase as they approach the Mach disk. The barrel shock and the Mach disk are marked by the red areas of high density change. In Fig. 7 the z component of density change $\mathrm{d}\rho/\mathrm{d}z$ is given on the jet centerline. The density gradients are at their steepest at jet exit and in the proximity of the Mach disk. The position of the Mach disk is localized by the minimum of the density gradient distribution at $z_M/d_J = 6.91$ and concurs with the result of schlieren measurement (Fig. 5).

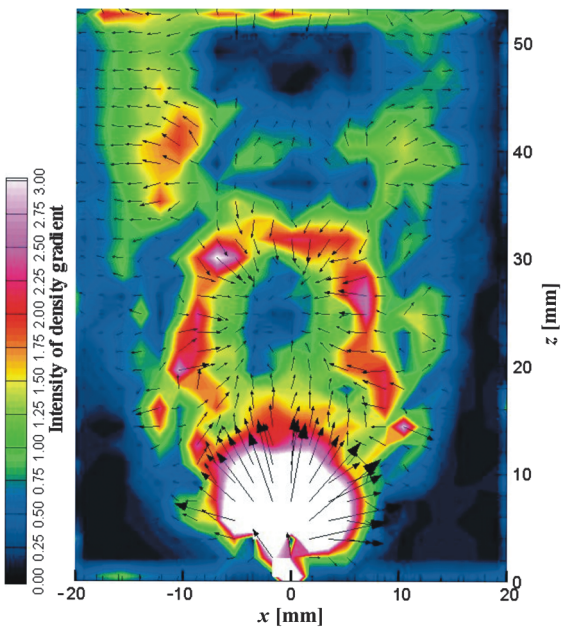

Fig. 6 Intensity and direction of density gradients in a cold side jet, $I = 134$ N and $d_J = 4.6$ mm.

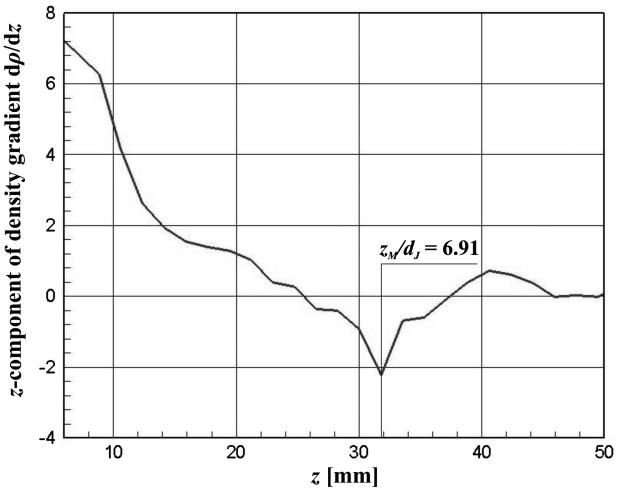

Fig. 7 Density gradient distribution at centerline of cold side jet, $I = 134$ N, $d_J = 4.6$ mm.

If the visualization of the flowfield is confined to shocks, conventional schlieren imaging yields an undisputedly higher quality of shock depiction than the BOS method. The low resolution is attributable to the lack of sharpness of the speckle pattern with flow.

To visualize the shocks generated by side jets in a supersonic freestream, schlieren videos were recorded. Figure 8 shows the development of the shock structures of the cold- and hot-gas jets for different momentum flux values $(\rho_{\mathrm{JH}} \cdot U_{\mathrm{JH}}^2) \cdot A_J = (\rho_{\mathrm{JC}} \cdot U_{\mathrm{JC}}^2) \cdot A_J$ at jet exit. As a consequence of the high exit velocity of the hot-gas jet, deeper penetration into the freestream is recorded for lower momentum flux values. Furthermore, with increasing exit momentum flux the schlieren images show a considerably greater extension of the separation area upstream from the nozzle. At a jet momentum flux of 134 N, the barrel shock, Mach disk, and recompression shock

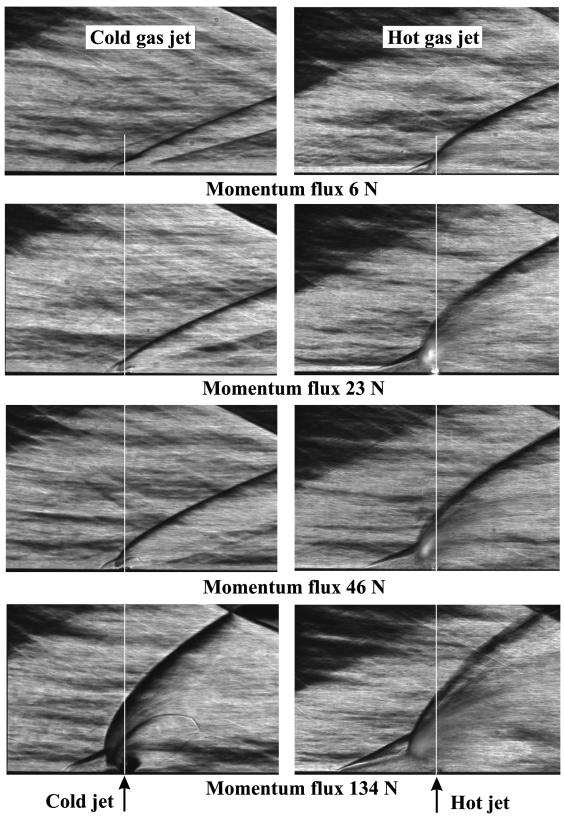

Fig. 8 Schlieren visualization of the shock development of a cold and hot side jet at different momentum flux $M_\infty = 3.0$, $Re_D = 14 \times 10^6$, 3 kfps, and $\alpha = 0°$.

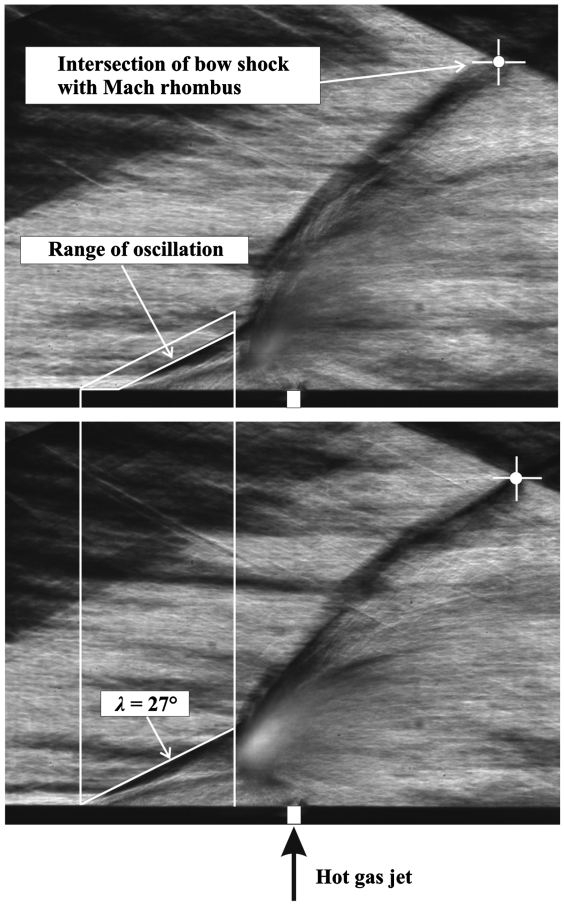

Fig. 9 Schlieren visualization of the oscillating separation and bow shock of hot-gas jet, $M_\infty = 3.0$, $Re_D = 14 \times 10^6$, $I = 134$ N, 3 kfps, and $\alpha = 0°$.

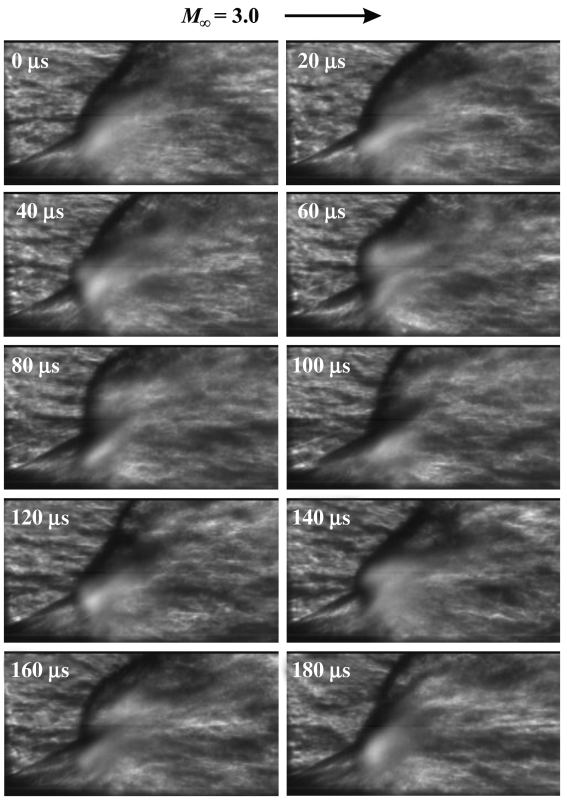

Fig. 10 Schlieren visualization of the oscillating separation and bow shock of hot-gas jet, $M_\infty = 3.0$, $Re_D = 14 \times 10^6$, $I = 134$ N, 50 kfps, and $\alpha = 0°$.

are visible for the cold gas, while for the hot-gas jet these shock structures are masked by the jet's shear layer (Fig. 5). The hot-gas schlieren video also shows strong oscillation of the bow and separation shocks. To visualize the oscillation of the separation shock, the range of oscillation is marked in Fig. 9. Viewed axially, the separation range of the separation shock alternates by ±9% about the mean separation point.

To facilitate a detailed analysis of the shock oscillations, a high-speed schlieren video at 50 kfps with resolution of 259 × 128 pixels was recorded. The strong oscillations of the bow shock can be clearly seen in Fig. 10. To determine the oscillation frequency of the shock structure, the following image processing steps were used. Each recorded image was thus compared to the neighboring images up to a specific distance forward and backward in time. The sum of the absolute difference in pixels for each image pair was used as the correlation function. The oscillation of the shock system was calculated from the minima and maxima of these correlations over time for each series. This analysis was performed in an automated process for every 100th of the recorded 100,000 images for distances of up to ±128 images. The strong frequency noise of the measurement does not express oscillation variation in the gas jet, but mostly expresses the high noise level in the images as well as the sometimes-strong variations between each oscillation, so only averaged values of the measurements were used for the analysis.

The evaluation of the high-speed schlieren video according to this algorithm in Fig. 11 shows that the separation and bow shock of the fully developed hot-gas jet oscillate on average at 11.3 kHz throughout the combustion process. This oscillation frequency is not excited by resonances in the combustion chamber, but is generated by the interaction of the hot-gas jet with the freestream. The axial resonances in the combustion chamber amount to about 9.5 kHz at the start of burn. Toward the end of burn, the length of the combustion chamber has grown by a factor of 2, causing the resonance frequency to fall to 4.7 kHz. Since these frequencies are significantly below the oscillation frequency of the shocks, the excitation of the shock oscillations by processes in the combustion chamber can be excluded.

Figure 12 compares the schlieren images taken at angles of attack of $\alpha = 10$, 0, and $-10°$ and the same exit momentum flux. Particularly when $\alpha = 10°$, the area in front of the hot-gas jet is significantly larger than that of the cold-gas jet. When $\alpha = 0$ and $-10°$, the differences in the overpressure areas are less strongly manifested.

C. Wall Pressure Measurements

The comparison of the shock structures of the cold- and hot-gas jets reveals striking changes in the flow topology. Supplementing the topology, the wall pressure distributions published in [7] are thus presented in Fig. 13. The freestream Mach number was $M_\infty = 3.0$ and the jet pressure ratio was the same for both configurations: $p_{tH}/p_\infty = p_{tC}/p_\infty = 220$. The pressure coefficient is calculated with the measured pressure data:

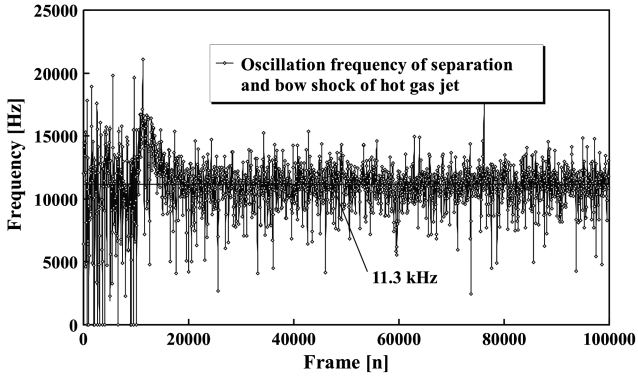

Fig. 11 Oscillation frequency of the separation and bow shock of a hot-gas jet, $M_\infty = 3.0$, $Re_D = 14 \times 10^6$, $I = 134$ N, 50 kfps, and $\alpha = 0°$.

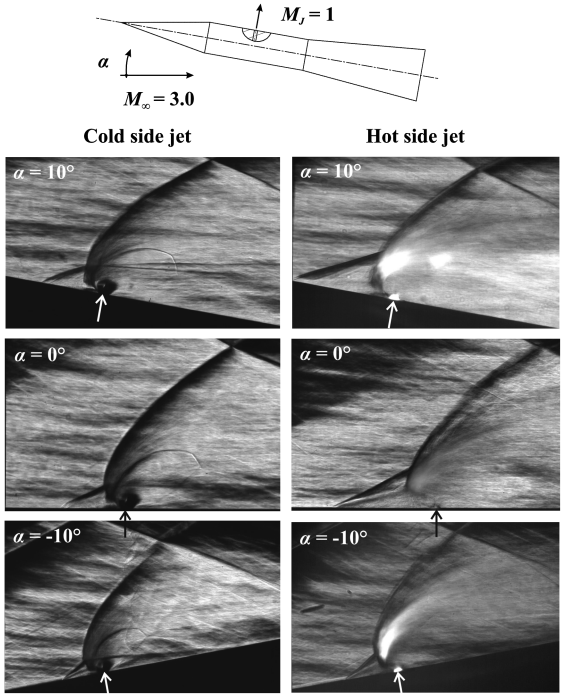

Fig. 12 Schlieren visualization of the shock structure at various angles of attack, $M_\infty = 3.0$, $Re_D = 14 \times 10^6$, $I = 134$ N, and 3 kfps.

$$C_{p\text{dif}} = 2 \cdot (p - p_\infty)/(p_\infty \cdot \kappa \cdot M_\infty^2) \qquad (2)$$

In the upstream separation region, the hot-gas jet causes a significant enlargement of the high-pressure area, according to the schlieren pictures (Fig. 12): i.e., the induced normal force in the direction of the jet increases and reinforces the thrust. In the wake of the jet, the low-pressure area is confined to a much smaller region. This means that the force against the jet thrust is markedly lower. If one considers the pressure distribution at the jet's position, starting at $\varphi = 180°$ in the circumferential direction, the hot-gas jet causes a shift in the induced high pressure toward larger circumferential angles. The maximum pressures differ by approximately $\Delta\varphi = 30°$. Here again, the pressure level is higher overall compared to the cold-gas jet. The complete pressure field in the interaction area of the side jets is given in [7].

The wall pressure distributions given in Fig. 13 were recorded at the same jet pressure ratio for the hot and cold jets. If the same exit momentum flux $I = 134$ N of the two configurations is defined as the boundary condition, the chamber pressure $p_{tC} = 112$ bar given in Table 2 has to be adjusted accordingly for the cold-gas jet. For the hot-gas jet employed in the present report, the combustion chamber pressure $p_{tH} = 120$ bar is dictated by the nozzle diameter $d_J =$ 4.6 mm. The jet pressure ratio is then $p_{tH}/p_\infty = 220$ for the hot-gas jet and $p_{tC}/p_\infty = 205$ for the cold-gas jet and is thus 7% smaller. According to studies by Esch [13], the deviations from the target value of $\leq 6\%$ for the jet pressure ratio cannot be detected in the wall pressure distributions. Compared to the wall pressure distributions presented in Fig. 13, the difference in the wall pressure distributions would tend to be slightly larger in the area in front of the jet and in the wake and, on the other hand, slightly smaller for the pressure distributions measured with the same momentum flux [21]. With the same thrust as the boundary condition, no differences can be detected from the wall pressure distributions recorded at the same jet pressure ratio.

Figure 14 shows the model surface after a hot-gas test. As a result of combustion residues from the solid propellant, the overpressure area in front of the jet and the low-pressure area in the wake are marked. The separation of the boundary layer takes place about 10 nozzle diameters upstream and is marked on the associated wall pressure distribution by a dot. In the wake of the hot-gas jet, the area of low pressure is documented approximately by boundary lines.

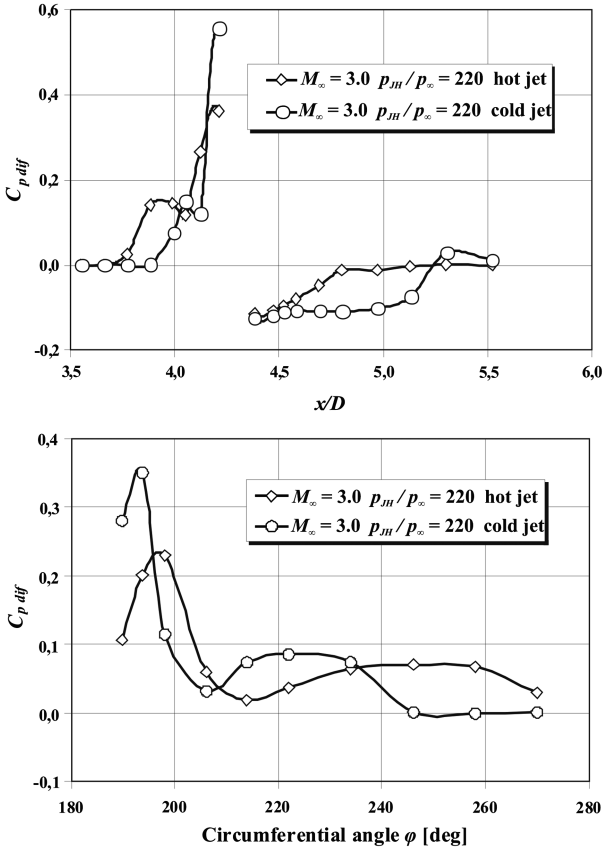

Fig. 13 Effect of a hot-gas jet on pressure distribution in the side-jet interaction region, $Re_D = 14 \times 10^6$, $T_t = 293$ K, $T_\infty = 103$ K, and $\alpha = 0°$ (Stahl et al. [7]).

D. High-Speed Videos of the Hot Side Jet

To analyze the interaction of a hot-gas jet in a supersonic freestream, high-speed videos were taken (without schlieren imaging) at 50 kfps (256 × 128 pixels) in a range of angles of attack of $-10° \leq \alpha \leq 10°$. From these videos, video sequences were extracted and averaged over 500 frames. Figure 15 shows the pronounced inclination of the jet plume upstream from the nozzle.

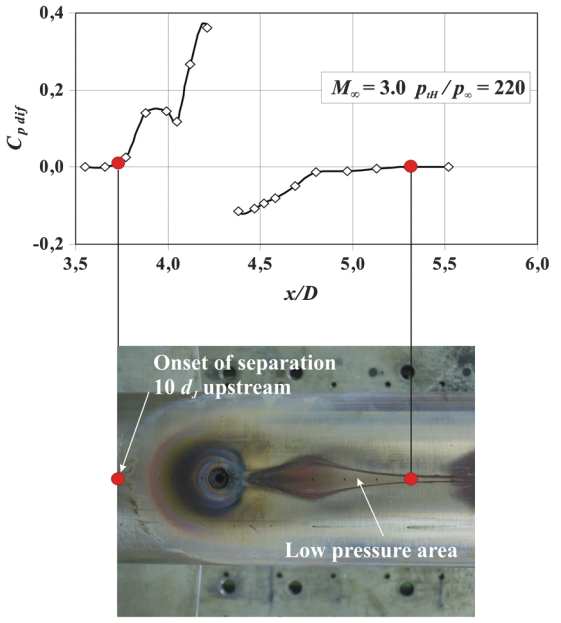

Fig. 14 Onset of separation in front of the hot-gas jet and low-pressure area in the wake, $Re_D = 14 \times 10^6$, $t_t = 293$ K, $T_\infty = 103$ K, $I = 134$ N, $\alpha = 0°$, and $d_J = 4.6$ mm.

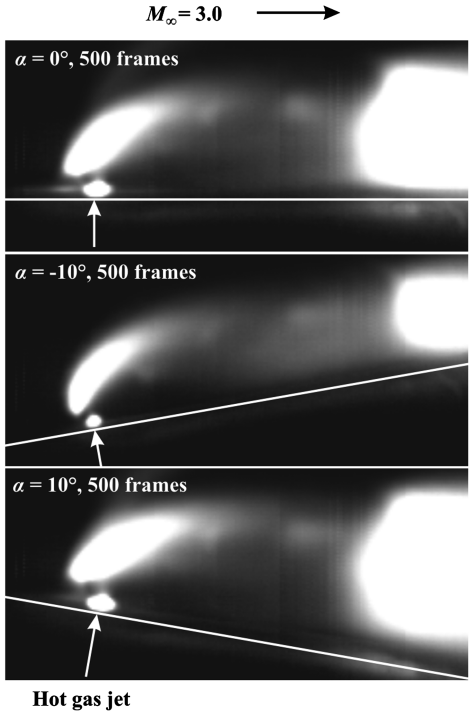

Fig. 15 Illustration of the hot-gas jet averaged over 500 frames, $M_\infty = 3.0, Re_D = 14 \times 10^6, I = 134$ N, 50 kfps, $\Delta t = 20$ μs, and $\alpha = 0°$.

This phenomenon is due to the screening-off of the hot-gas jet by the dominant shocks in front of the jet. In this area, Eichhorn and Emunds [16] ascertained the maximum jet temperatures with rotational spectra of copper hydride.

A look at the development of a hot-gas jet at the start of the video recording at intervals of $\Delta t = 2$ ms in Fig. 16 reveals evidence of pronounced periodicity. To determine this oscillation frequency, a video taken at $\alpha = 0°$ was evaluated with the aid of the algorithm given above. Concurring with the evaluated shock oscillations, the oscillation of the hot jet plume comes to a mean 11.3 kHz (Fig. 17). The noise level here is lower than that obtained from the evaluation of the shock oscillations (Fig. 11), because the jet plume is screened off from the separation and bow shock. If the images of a video sequence are viewed individually, it is possible to follow the convection of large-scale structures (Fig. 18). To determine their convection velocities, the displacement of the structure was manually evaluated. Figure 19 shows the development of large-scale structures in the streamwise direction in an x-t diagram. The translation of a vortex was evaluated, as given in Fig. 18 as an example, with 256×128 pixels from the nozzle to the end of the measuring field. It was possible to evaluate up to a maximum of 13 frames: i.e., vortex movements in the x and z directions. For an angle of attack of $\alpha = 10°$, evaluation was limited to eight frames, as the jet expanded strongly downstream and the vortex structures could no longer be identified with precision. With a displacement of the structures between images and for the known interframing time of $\Delta t = 20$ μs, the large-scale convection velocities are determined using

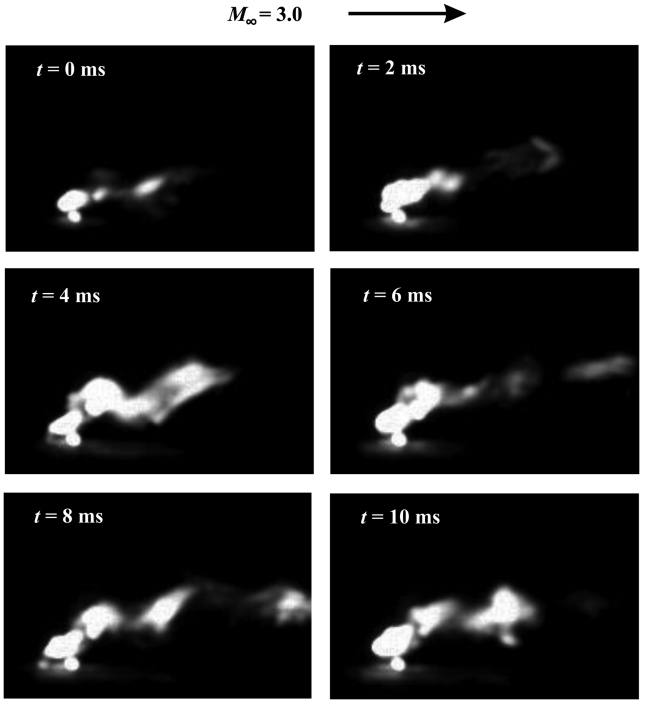

Fig. 16 Development of the hot-gas jet in a supersonic freestream, $Re_D = 14 \times 10^6, I = 134$ N, 50 kfps, $\Delta t = 20$ μs, and $\alpha = 0°$.

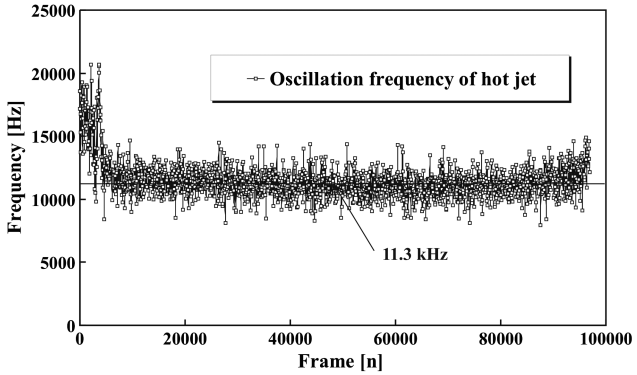

Fig. 17 Frequency of hot jet oscillation, $M_\infty = 3.0$, $Re_D = 14 \times 10^6$, $I = 134$ N, 50 kfps, $\Delta t = 20$ μs, and $\alpha = 0°$.

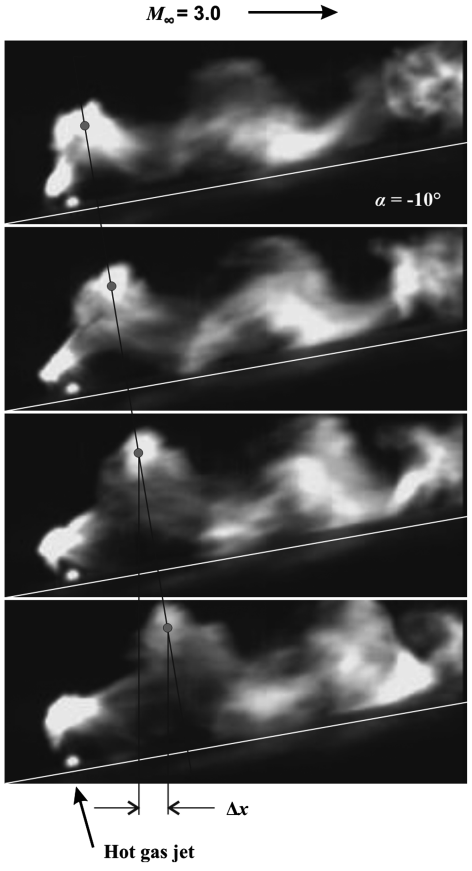

Fig. 18 Video sequence of large-scale structures of a full developed hot-gas jet, $Re_D = 14 \times 10^6, I = 134$ N, 50 kfps, $\Delta t = 20$ μs, and $\alpha = -10°$.

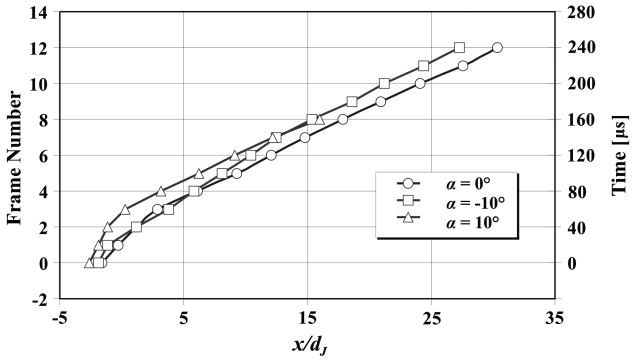

Fig. 19 Space–time trajectories of large-scale structures at different angles of attack.

$$U_{cx} = (x_2 - x_1)/\Delta t, \qquad U_{cz} = (z_2 - z_1)/\Delta t \tag{3}$$

and

$$U_c = (U_{cx}^2 + U_{cz}^2)^{1/2} \tag{4}$$

The convection angle Φ associated with these velocities can be computed from the following trigonometric ratio:

$$\Phi = \arctan[(z_2 - z_1)/(x_2 - x_1)] \tag{5}$$

The expressions presented above are used to determine the structures' convective characteristics.

Figure 20 shows the convection velocities of the vortices in x and z directions for three of the model's angles of attack. These plots also contain velocity reference lines that indicate the freestream velocity $U_\infty = 613$ m/s and the jet exit velocity $U_J = 900$ m/s. The error possible due to manual evaluation was estimated to be ± 30 m/s and was documented for both coordinates at the measuring points. In the proximity of the nozzle there is a significant increase in convection velocities, particularly when $\alpha = -10$ and 10° in both the x and y directions. Further downstream, the axial convection velocities U_{cx} mainly exceed freestream velocity. This phenomenon is attributable to the expansion of the hot-gas jet outside the nozzle. At $x/d_J \approx 15$ the lateral convection velocities U_{cz} converge toward zero, because the hot-gas jet becomes increasingly aligned with the direction of freestream. Finally, Fig. 21 shows the convection velocities U_c and the associated convection angle Φ calculated from the two velocity components. Remarkable here is the significant increase in the convection velocities in the exit area for all of the model's angles of attack. The convection velocities measured at higher jet pressure ratio and published in [7] concur well in the case of $\alpha = 0°$ with the results of Fig. 20. The convection angles approximate to the direction of freestream after only about 10 nozzle diameters.

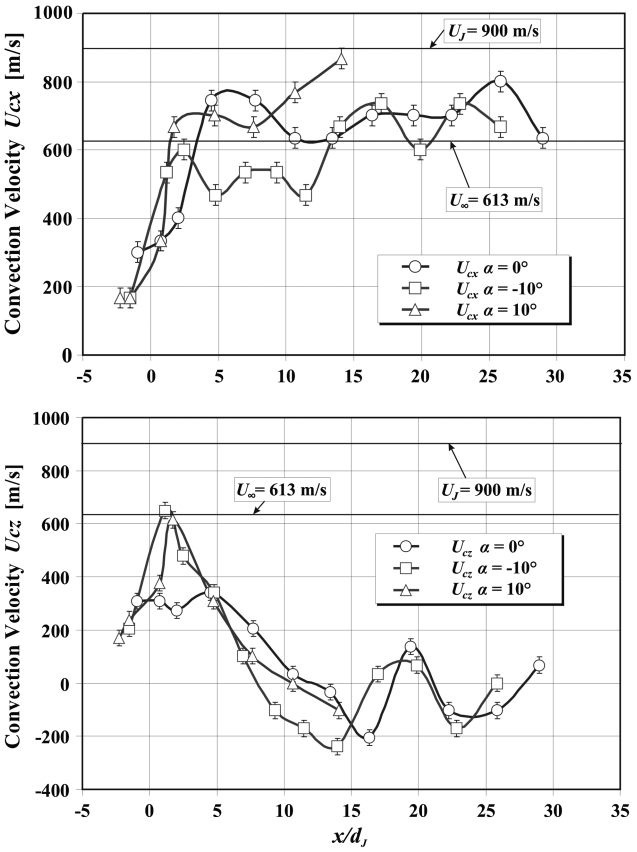

Fig. 20 Convection velocity distributions of large-scale structures in a hot-gas jet at various angles of attack.

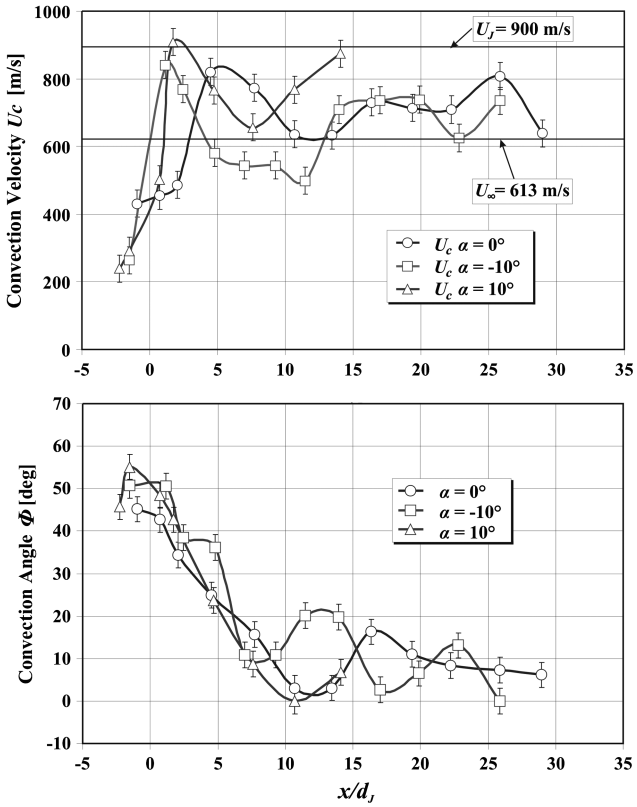

Fig. 21 Convection velocity U_c distribution of large-scale structures and their convection angles, measured at $M_\infty = 3.0$, $Re_D = 14 \times 10^6$, and $I = 134$ N, 50 kfps.

IV. Conclusions

An experimental study was carried out on a high-speed missile in the interaction range of cold and hot side jets in a supersonic freestream. To this end, high-speed schlieren videos were recorded to detect shocks. From these recordings, it can be concluded for the case without a freestream that the hot-gas jet has a much thicker shear layer than the cold-gas jet. The distance from the nozzle to the Mach disk is about the same for both jets. Schlieren images taken with a superimposed freestream show pronounced oscillation of the shocks in the area in front of the hot-gas jet. By applying an algorithm that analyzes the similarity of neighboring video images, the oscillation frequency of the separation and bow shock was calculated to be 11.3 kHz on average. The schlieren images also show that the area in front of the hot-gas jet extends much further upstream than that of the cold-gas jet. This overpressure area was quantitatively confirmed with wall pressure measurements. Furthermore, to analyze the structure and propagation of the jet plume, high-speed videos were taken at 50 kfps and the development of large-scale vortex structures was detected in the hot-gas jet. These vortices oscillate in accordance

with the oscillations of the shocks at a frequency of 11.3 kHz. The jet plume oscillations are not triggered by resonances from the combustion chamber but are generated by the jet's interaction with the freestream. By averaging video sequences over 500 frames, a considerable inclination of the jet plume was detected upstream from the nozzle. This phenomenon is attributable to the screening-off of the jet plume by the dominant separation and bow shock in the area in front of the jet. Finally, the convection velocities of large-scale vortices were determined from video sequences. Immediately at the exit of the hot-gas jet, there is a significant increase in the convection velocities as a consequence of the jet's expansion. Downstream, the convection velocities mainly range between freestream velocity and the hot-gas jet's exit velocity.

Acknowledgments

The authors would like to acknowledge the support of the German Ministry of Defense for this work. We highly appreciate the support of J. Klinner for the background-oriented schlieren measurements and data reduction. In addition, we thank the supplier of the propellants, the company Bayern-Chemie of Aschau, Germany, for the information about the composition of the hot gas. For this, B. Esser kindly calculated the isentropic exponent and gas constant.

References

[1] Gnemmi, P., and Schäfer, H. J., "Experimental and Numerical Investigations of a Transverse Jet Interaction on a Missile Body," French–German Inst. of Saint-Louis, Saint-Louis, France, Rept. PU 603/2005, 2005.

[2] Gnemmi, P., and Seiler, F., "Interaction of a Lateral Jet with the Projectile Cross-Flow," AIAA Paper 2000-4196, 2000.

[3] Havermann, M., Ende, H., Seiler, F., and Schwenzer, M., "Shock Tunnel Measurements of the Interaction Amplification Factor for a Hot Gas Side Jet in a Supersonic Cross-Flow," *Proceedings of the International Symposium on Shock Waves*, Vol. 1, 2005.

[4] Ben-Yakar, A., Mungal, M. G., and Hanson, R. K., "Time Evolution and Mixing Characteristics of Hydrogen and Ethylene Transverse Jets in Supersonic Cross-Flows," *Physics of Fluids*, Vol. 18, 2006, Paper 026101.
doi:10.1063/1.2139684

[5] Champigny, P., and Lacau, R. G., "Lateral Jet Control for Tactical Missiles," AGARD Rept. 804, Neuilly-sur-Seine, France, 1994, pp. 3-1–3-57.

[6] Gnemmi, P., Eichhorn, A., Emunds, H., Esch, H., Gülhan, A., Leopold, F., and Schäfer, H. J., "Experimental and Computational Study of the Interaction Between a Lateral Jet and the Supersonic Cross-Flow on a Generic Missile Body," *Innovative Missile Systems*, RTO-AMP-AVT-135, NATO, Amsterdam, May 2006.

[7] Stahl, B., Emunds, H., and Gülhan, A., "Experimental Investigation of Hot and Cold Side Jet Interaction with a Supersonic Freestream," *Journal of Aerospace Science and Technology*, Vol. 13, No. 8, Dec. 2009, pp. 423–496.
doi:10.1016/j.ast.2009.06.002

[8] Spaid, F. W., and Cassel, L. A., "Aerodynamic Interference Induced by Reaction Controls," AGARD Rept. AG-173, Neuilly-sur-Seine, France, 1973, pp. 1–62.

[9] Chamberlain, R., McClure, D., and Dang, A., "CFD Analysis of Lateral Jet Interaction Phenomena for the THAAD Interceptor," 38th AIAA Aerospace Sciences Meeting & Exhibit, AIAA Paper 2000-0963, Reno, NV, 2000.

[10] Esch, H., "Kraftmessungen an einem TLVS-Modell mit Heißgas-Querschubsimulation," DLR, German Aerospace Center Rept. IB-39113-94C08, Cologne, Germany, 1994.

[11] Naumann, K. W., Ende, H., George, A., and Mathieu, G., "Shock-Tunnel Experiments on Lateral Jet Interaction. Methods and Results," 32nd AIAA/ASME/SAE/ASEE, Joint Propulsion Conference, AIAA Paper 96-2690, Lake Buena Vista, FL, July 1996.

[12] Mahmud, Z., and Bowersox, R. D. W., "Aerodynamics of Low-Blowing-Ratio Fuselage Injection into a Supersonic Free-Stream," *Journal of Spacecraft and Rockets*, Vol. 42, No. 1, Jan.–Feb. 2005, pp. 30–37.
doi:10.2514/1.4803

[13] Esch, H., "Querschubstrahl-Interferenzen an einem Flugkörperrumpf im Überschall bei unterschiedlichen Ausblasmedien," DLR, German Aerospace Center Rept. IB-39113-99C27, Cologne, Germany, 1999.

[14] Gülhan, A., Schütte, G., and Stahl, B., "Experimental Study on Aerothermal Heating Caused by Jet-Hypersonic Freestream Interaction," *Journal of Spacecraft and Rockets*, Vol. 45, No. 5, Sept.–Oct. 2008, pp. 891–899.
doi:10.2514/1.35899

[15] Ashkenas, H., and Sherman, F. S., "The Structure and Utilization of Supersonic Free Jets in Low Density Wind Tunnels," *Rarefied Gas Dynamics*, Vol. 2, Academic Press, New York, 1966, pp. 84–105.

[16] Eichhorn, A., and Emunds, H., "Neue Experimente zur Spektroskopischen Temperaturbestimmung im Heißgasstrahl. Ermittlung der Temperatur aus dem Spektrum von Kupferhydrid (CuH)," French–German Inst. of Saint-Louis, Saint-Louis, France, Rept. R 110/2007.

[17] Goldhahn, E., and Seume, J., "The Background Oriented Schlieren Technique, Sensitivity, Accuracy, Resolution and Application to a Three-Dimensional Density Field," *Experiments in Fluids*, Vol. 43, 2007, pp. 241–249.
doi:10.1007/s00348-007-0331-1

[18] Richard, H., and Raffel, M., "Principle and Applications of the Background Oriented Schlieren (BOS) Method," *Measurement Science and Technology*, Vol. 12, No. 9, 2001, pp. 1576–1585.
doi:10.1088/0957-0233/12/9/325

[19] Venkatakrishnan, L., "Density Measurements in an Axisymmetric Underexpanded Jet by Background-Oriented Schlieren Technique," *AIAA Journal*, Vol. 43, No. 7, July 2005, pp. 1574–1579.
doi:10.2514/1.12647

[20] Leopold, F., Simon, J., Gruppi, D., Schäfer, H. J., "Recent Improvements of the Background Oriented Schlieren Technique (BOS) by Using a Coloured Background," French–German Inst. of Saint-Louis, Saint-Louis, France, Rept. PU-627/2006.

[21] Stahl, B., Esch, H., and Gülhan, A., "Experimental Investigation of Side Jet Interaction with a Supersonic Cross-Flow," *Journal of Aerospace Science and Technology*, Vol. 12, No. 4, 2008, pp. 269–275.
doi:10.1016/j.ast.2007.01.009

M. Miller
Associate Editor